He I Ultraviolet Photoelectron Spectroscopy of Benzene and Pyridine in Supersonic Molecular Beams Using Photoelectron Imaging

Suet-Yi Liu,[†,‡] Koutayba Alnama,[†] Jun Matsumoto,[†,⊥] Kiyoshi Nishizawa,[†] Hiroshi Kohguchi,[†,§] Yuan-Pern Lee,[‡] and Toshinori Suzuki*,[†,‡,‖]

[†]Chemical Dynamics Laboratory, RIKEN Advanced Science Institute, 2-1 Hirosawa, Wako 351-0198, Japan

[‡]Department of Applied Chemistry, National Chiao Tung University, Hsinchu 30010, Taiwan

[§]Department of Chemistry, School of Science, Hiroshima University, 1-3-1 Kagamiyama, Higashi-Hiroshima 739-8526, Japan

[‖]Department of Chemistry, Graduate School of Science, Kyoto University, Kyoto 606-8502, Japan

Ⓢ Supporting Information

ABSTRACT: We performed He I ultraviolet photoelectron spectroscopy (UPS) of jet-cooled aromatic molecules using a newly developed photoelectron imaging (PEI) spectrometer. The PEI spectrometer can measure photoelectron spectra and photoelectron angular distributions at a considerably higher efficiency than a conventional spectrometer that uses a hemispherical energy analyzer. One technical problem with PEI is its relatively high susceptibility to background electrons generated by scattered He I radiation. To reduce this problem, we designed a new electrostatic lens that intercepts background photoelectrons emitted from the repeller plate toward the imaging detector. An energy resolution ($\Delta E/E$) of 0.735% at $E = 5.461$ eV is demonstrated with He I radiation. The energy resolution is limited by the size of the ionization region. Trajectory calculations indicate that the system is capable of achieving an energy resolution of 0.04% with a laser if the imaging resolution is not limited. Experimental results are presented for jet-cooled benzene and pyridine, and they are compared with results in the literature.
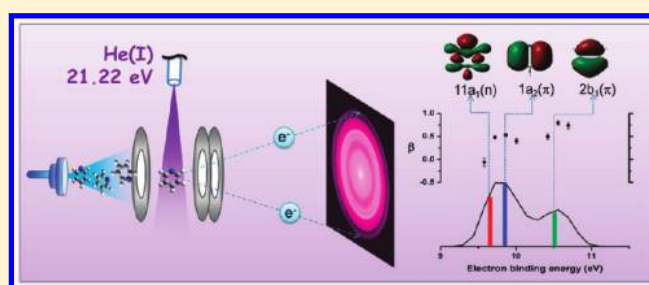
INTRODUCTION

He I ultraviolet photoelectron spectroscopy (UPS) was first developed in the early 1960s,[1,2] and it has been offering invaluable insights into the electronic structures of molecules. The photoelectron kinetic energy distribution measured by UPS reveals the electronic energy level structure of a cation, which is also related to the electron orbital energies of a neutral molecule within Koopmans' approximation.[3] The vibrational fine structure associated with each ionization band indicates the bonding character of the electron orbital from which an electron has been removed; this permits a molecular orbital to be assigned to each photoelectron band.[4] An ultraviolet photoelectron spectrometer with a high-performance hemispherical electron energy analyzer and an intense He I lamp using the electron cyclotron resonance[5] has achieved an impressively high spectral resolution ($\Delta E < 5$ meV) that is limited only by the line width of the He I radiation. However, a hemispherical energy analyzer has a small electron acceptance angle and a limited energy range observed simultaneously; these factors severely limit the signal count rate. Consequently, UPS has been scarcely applied to highly diluted gases in supersonic molecular beams[6] and biological molecules that could not be prepared in a large quantity.

Even at the highest spectral resolution achieved using a hemispherical energy analyzer,[7,8] UPS fails to match the resolution accomplished by pulsed-field-ionization zero-kinetic-energy photoelectron spectroscopy (PFI-ZEKE).[9,10] PFI-ZEKE observes the resonances of the photon energy with the rovibronic energies of Rydberg states associated with each cation state.[11,12] It utilizes the fact that Rydberg states with high principal quantum numbers are structurally similar to a cationic state due to the weak coupling between the Rydberg electron and the ion core. PFI-ZEKE requires these Rydberg states to be long-lived; it thus encounters difficulties when the Rydberg states rapidly dissociate or undergo autoionization.[13] The higher excited states of a cation, corresponding to electron removal from inner valence orbitals, tend to exhibit inherently broad photoelectron bands, indicating the existence of rapid deactivation processes. Therefore, PFI-ZEKE may not be the best approach for investigating these states.[13] In this sense, He I UPS and PFI-ZEKE can be regarded as being complementary.

One advantage of UPS over PFI-ZEKE is that UPS can be used to investigate the angular distribution of photoelectrons. The photoelectron angular distribution (PAD) is a useful tool in UPS. For example, Carlson and Anderson[14] performed He I UPS of benzene in 1971 and found that its photoelectron bands exhibit characteristic angular anisotropy. This helped them to analyze
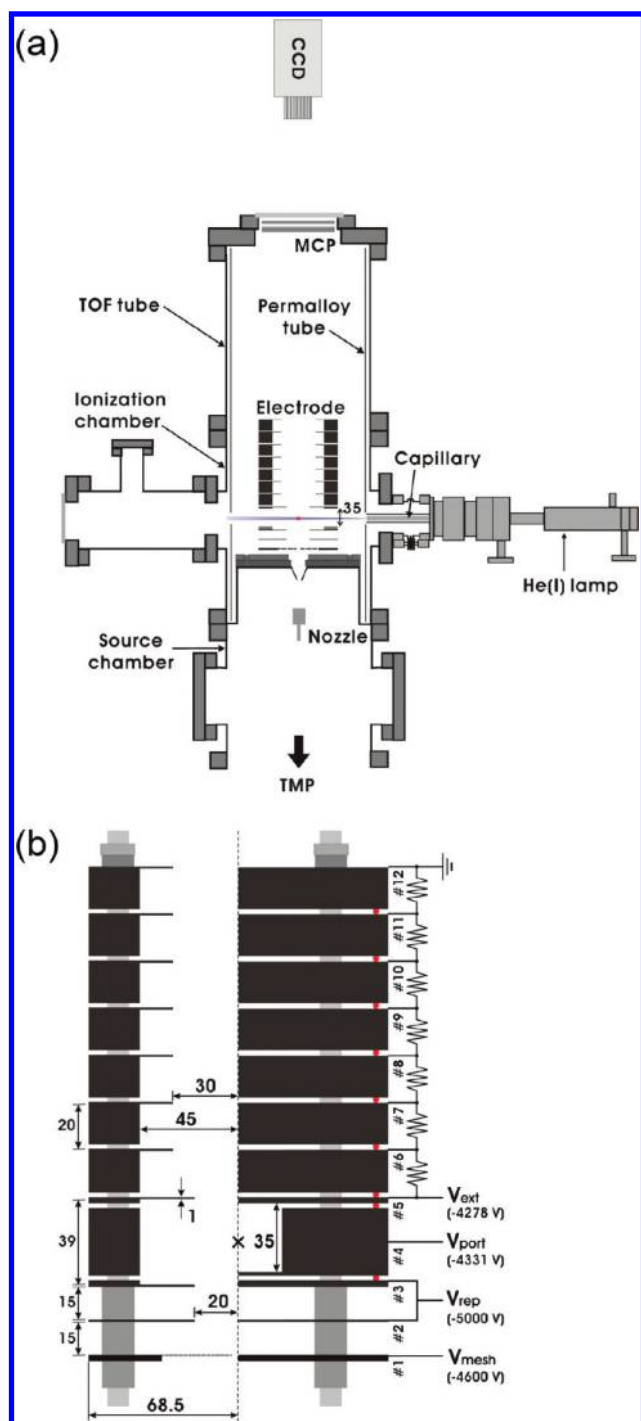
Figure 1. (a) Cross-sectional view of our experimental setup. The dimensions in this drawing are proportional to the real sizes. (b) Cross-sectional view (left half) and front view (right half) of our electrostatic lens system (all units in millimeters). A molecular beam is introduced from the bottom and is irradiated by He I radiation at the position indicated by the cross ($\times$). Electrodes 1–3 were spaced by a plastic insulator, whereas electrodes 3–12 were spaced by 3 mm diameter ruby balls (indicated by red circles). The figure also shows an example of the voltage settings for obtaining a photoelectron image of Kr.

the overlapping bands in the spectrum. The occurrence of overlapping photoelectron bands is an inherent characteristic of photoelectron spectroscopy of polyatomic molecules with many valence electrons. As mentioned above, when the

vibrational structure of each photoelectron band can be resolved, it can be used for spectral assignment. However, when the structure cannot be resolved (as is the case for inner valence photoionization), PAD is valuable for characterizing the orbital from which an electron is removed. The measurement of the photon-energy dependence of PAD is even more useful for assignments.[15]

In this study, we report a He I photoelectron imaging (PEI) spectrometer[16] that provides the ultimate collection efficiency of photoelectrons of 4π steradians and efficient measurement of PADs. We use this novel spectrometer to perform UPS of the benchmark systems of benzene and pyridine in supersonic molecular beams. One disadvantage of PEI compared with a hemispherical energy analyzer is its relatively high susceptibility to background photoemission from the instrument by scattered He I radiation. To overcome this difficulty, we designed a new electrostatic lens that intercepts background photoelectrons emitted from an electrode of PEI toward an imaging detector. Compared with a hemispherical energy analyzer, a PEI spectrometer achieves a considerably higher electron collection efficiency at the expense of a lower energy resolution; however, we demonstrate that an energy resolution of 0.735% is obtainable.

The PEI spectrometer developed in this study for He I radiation is applicable to photoelectron spectroscopy with other vacuum ultraviolet (VUV) sources besides He I; such sources include synchrotron radiation, free electron lasers (FELs),[17−19] and high harmonics generated by ultrashort pulsed lasers.[20−22] In fact, PEI is considerably more difficult with incoherent He I light than coherent photon beams as the former cannot be tightly focused on a sample.

■ EXPERIMENT

A. Molecular Beam Chambers and Imaging System. Figure 1a shows the cross-sectional view of our experimental setup with the dimensions proportional to real sizes. We used a continuous or pulsed molecular beam depending on the experiment. In the former case, a continuous supersonic jet was generated by expanding a sample gas from a 25 μm diameter orifice at 294 K. The jet was skimmed with a 0.8 mm diameter skimmer and introduced into an ionization chamber. The source and ionization chambers were pumped by turbomolecular pumps with pumping rates of 2000 L/s (N_2) and 820 L/s (N_2), respectively. When Ar was continuously expanded at a stagnation pressure of 1 atm, the ionization chamber pressure was ca. 7.3×10^{-8} Torr. He I radiation at 21.22 eV (58.4 nm) was generated using a commercial discharge lamp (Omicron, HIS13) and it was transmitted through a 0.8 mm diameter capillary. The end of the capillary was located ∼125 mm from the ionization point. The photon flux is 9.4×10^{10} (photons/s)/mm^2 at the sampling point. Electrons generated by photoionization of a sample were accelerated along the molecular beam propagation axis and projected onto a 2D position-sensitive detector. The acceleration field was created using stacked circular ring electrodes and the field gradient was carefully adjusted to achieve a velocity mapping condition.[23] The details of the electrodes are described in the next section. The entire regions of photoionization, acceleration, and flight of the electrons were shielded against external magnetic fields by a permalloy tube. The position-sensitive detector consists of a chevron-type (dual) microchannel plate assembly (Hamamatsu, F1942-04; pore diameter, 25 μm; diameter,

77 mm) backed by a phosphor screen (P43) and a CCD camera (Andor, iXon^{EM} DCL897; 512×512 pixels).

In the time-gated experiments, 10−20% sample gases seeded in He were expanded from a pulsed valve (General Valve; orifice diameter: 100 μm) with a stagnation pressure of about 0.2−0.55 atm. The front surface of the microchannel plate (MCP) assembly was maintained at the ground potential and the voltage applied to the rear side was switched between 900 and 1400 V using a high voltage pulser (DEI, GRX-3.0K-H) to time-gate the MCP synchronously with a pulsed gas nozzle. The timing of the trigger pulses for the gas nozzle, MCP, and CCD camera was controlled with a digital delay generator (Stanford Research Systems, DG535).

B. Electrostatic Lens Design. Since He I radiation is incoherent with poor beam characteristics, its stray VUV light tends to generate considerable background photoemission from metal surfaces in the chamber, which interferes with VUV-PEI experiments. We estimated the angular divergence of the He I photon beam to be ±0.8°, which provides the 4.2 mm diameter of the He I radiation at the ionization point and 5.4 mm at the exit side of the electron acceleration lens. We have tested various electrodes and found that the hole should be at least 5 times larger than the estimated VUV beam diameter. This indicates that there is considerable intensity of a halo around the main (incoherent) VUV beam. To avoid the light scattering of this halo, holes as large as 40×35 mm rectangular size were made to electrode 4 in Figure 1b. While minimizing the scattering of VUV radiation described above, we have searched the source of background photoemission. We experimentally tested various electrode designs and also simulated electron trajectories computationally with the SIMION 3D software package (Scientific Instrument Services). These investigations revealed that a major component of the background photoemission originates from the repeller plate. Thus, we removed the solid repeller plate from our lens system.

As shown in Figure 1b, our final design of the lens system consists of a stack of 12 circular electrodes rigidly held by supporting rods made of insulator. The electrodes numbered 3−12 in the figure are spaced with 3 mm diameter ruby balls. We replaced one solid plate of a repeller with three components (nos. 1−3 in Figure 1b). Electrode 1 is made from a high-transmission (90%) mesh (70 wires/inch) with a 6 mm diameter hole in the center for the molecular beam to propagate through. The mesh reduces the cross-section of the electrode by 1 order of magnitude compared with a solid plate, which suppresses background photoemission from this electrode. Furthermore, the negative voltage of this electrode (no. 1) is set slightly lower in magnitude than that of electrodes 2 and 3 (see Figure 1b). This retardation prevents photoelectrons produced by stray light of VUV radiation from being transmitted toward the detector, as shown in Figure 2.

In Figure 1b, electrode 1 shields the acceleration fields against the ground potential. Electrode 2 is held at the same voltage as electrode 3 to avoid the field distortion caused by the large central hole in electrode 3. In the following, we refer to electrodes 3−5 as the repeller, light port, and extractor, respectively. Voltages were independently applied to electrodes 1−5 using a computer-controlled multiport power supply (MBS, A-1 Electronics; ±12 kV max), whereas the other electrode voltages were passively regulated by a register (22 MΩ) chain placed outside the vacuum chamber. The entire assembly can withstand voltages up to 12 kV (we used up to 11 kV in this study).
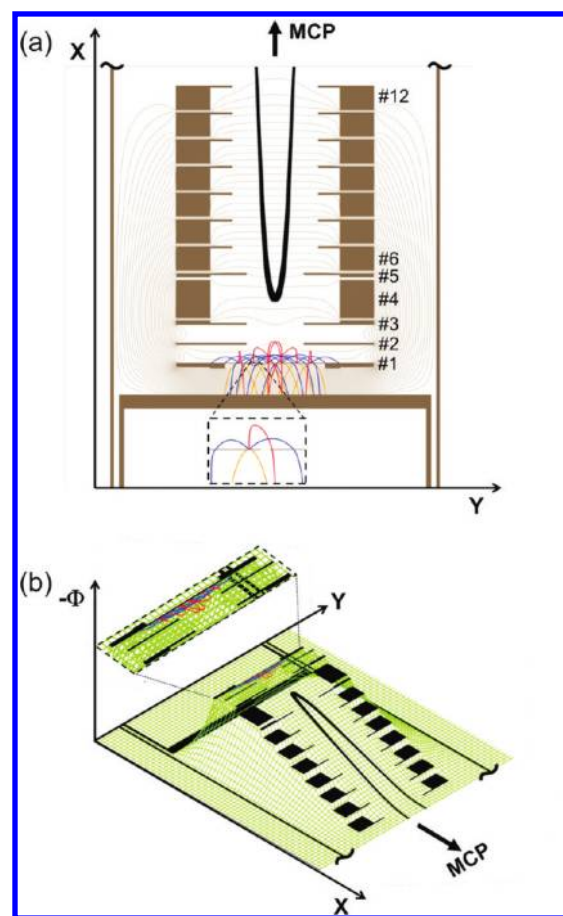
Figure 2. (a) Simulated trajectories (red, blue, and orange) of electrons emitted from the mesh electrode started from six different starting positions spaced 10 mm apart with five different ejection angles spaced by 45°: for enhancing the visibility of the trajectories, the kinetic energy of each electron was set to 200 eV. The inset shows an expanded view. The black curves are the trajectories of photoelectrons from the photoionization point, in which 500 electrons are ejected perpendicular to the flight axis (±Y axis direction) in the XY plane with 5.461 eV kinetic energy. The acceleration voltage on the repeller is −4000 V. The equipotential lines are also shown (light brown). (b) 2D representation of the cylindrically symmetric potential $\Phi(x,y)$ of (a). To show the turn-around trajectories of electrons emitted from the mesh electrode clearly, the trajectories of the electrons are stopped while they collided on the mesh electrode. The enlarged view of electrodes nos. 1− 3 is in the figure.

The gradual change in the voltages across the electrodes 5−12 results in "soft focusing" of the electron trajectories. The principle is essentially the same as the velocity map imaging by Eppink and Parker,[23] while the strength of the acceleration field varies much more gradually than the simplest design using three electrodes.[23] Previously, Lin et al.[24] have shown that soft focusing enlarges the source size of the charged particles from which their velocities can be focused on the detector. Lin et al. used an ion optics consisting of 29 rings, and obtained 10 mm o.d. (diameter) × 0.3 mm (thickness) of the ion/electron source from which the velocity can be mapped with the resolution ($\Delta v/v$) higher than 1%. We examined computationally the soft focusing effect with different numbers of lens electrodes in the acceleration region. Here we count the number of electrodes behind the extractor (lens no. 5): for instance, the electrodes shown in Figure 1b are

2955

dx.doi.org/10.1021/jp1098574 |*J. Phys. Chem. A* 2011, 115, 2953–2965
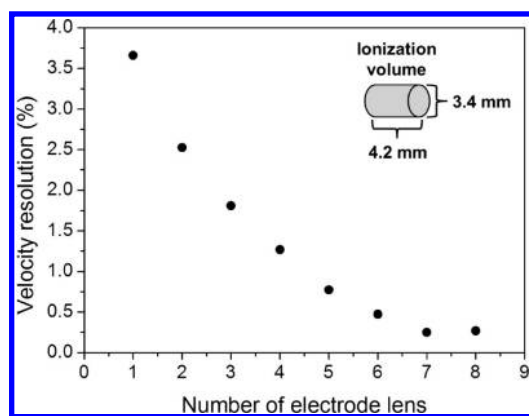
Figure 3. Calculated velocity resolution as a function of the number of lens electrodes behind the extractor. The ionization volume was assumed to be 3.4 o.d. × 4.2 mm. For each number of electrodes, the applied voltages were optimized to achieve the best resolution. The geometries of the electrodes are similar to Figure 1b except that the port electrode (no. 4 in Figure 1b) was removed. This was because the presence of the port electrode (no. 4) caused the voltage optimization to be a more complex procedure. The distance between the repeller (no. 3) and extractor (no. 5) was maintained with the original design.

12 in total whereas the lens electrodes behind the extractor are 7 (nos. 6−12). As shown in Figure 3, the calculated velocity resolution improves as more lens electrodes are employed; however, it was practically saturated at 7 electrodes. Therefore, we have decided to use 7 electrodes in our final design (Figure 1b). Ogi et al.[25] have reported the electrode assembly with 2 lens electrodes, which achieved a velocity resolution of 0.1%. However, it was with a small ionization volume created by a laser (o.d. 0.1 mm × 2 mm). On the other hand, our system with 7 lens electrodes described here achieves <0.37% for a considerably larger ionization volume.

■ RESULTS AND DISCUSSION

A. He I PEI of Rare Gases. The overlap between the molecular beam and the VUV light usually generates an approximately cylindrical ionization volume. We assumed that the molecular and VUV light beams were respectively 3.4 and 4.2 mm in diameter and examined the electron velocity resolution ($\Delta v/v$) by SIMION 3D. When the molecular beam has a diameter similar to or smaller than that of the VUV beam, the velocity resolutions parallel and perpendicular to the VUV beam are comparable. If the molecular beam has a diameter significantly larger than that of the VUV beam, the ionization volume becomes asymmetric and the resolutions in the two directions differ. The overall resolution of PEI is also limited by the imaging resolution, which is determined by the number of pixels of the camera and real-time processing such as centroiding calculations.

To fully exploit the performance of the charged particle optics, the imaging resolution should be sufficiently high. Figure 4 shows the photoelectron kinetic energy (PKE) distribution determined from an inverse Abel-transformed image of He I photoionization of Kr using a standard CCD camera (512 × 512 pixels) without any resolution enhancement processing. The spin−orbit splitting of Kr^+ (0.665 eV) is clearly resolved. The inset of Figure 4 shows an expanded view of the PKE region 6.0−8.0 eV together with a least-squares fit using a Gaussian function. The full width at half-maximum (fwhm) of the Gaussian, 0.210 eV, corresponds
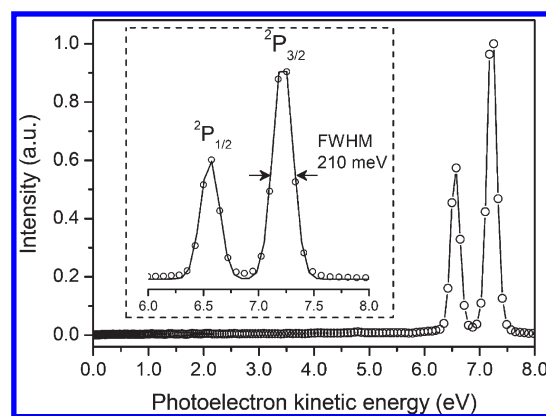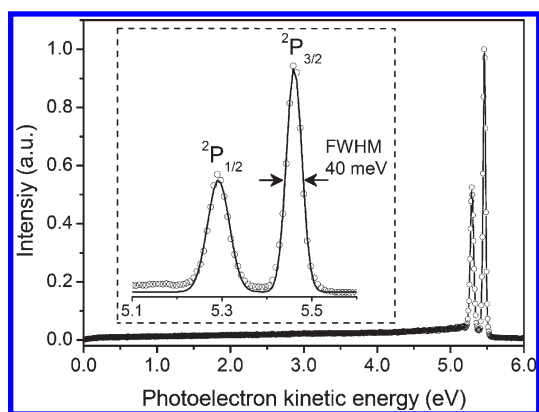

Figure 4. PKE distributions determined by He I PEI of supersonic beams of Kr using a 512 × 512 pixel CCD camera. The inset shows an expanded view in the PKE region between 6.0 and 8.0 eV. The solid line indicates the best-fit Gaussian to the observed data; it has a fwhm of 210 meV at 7.22 eV.
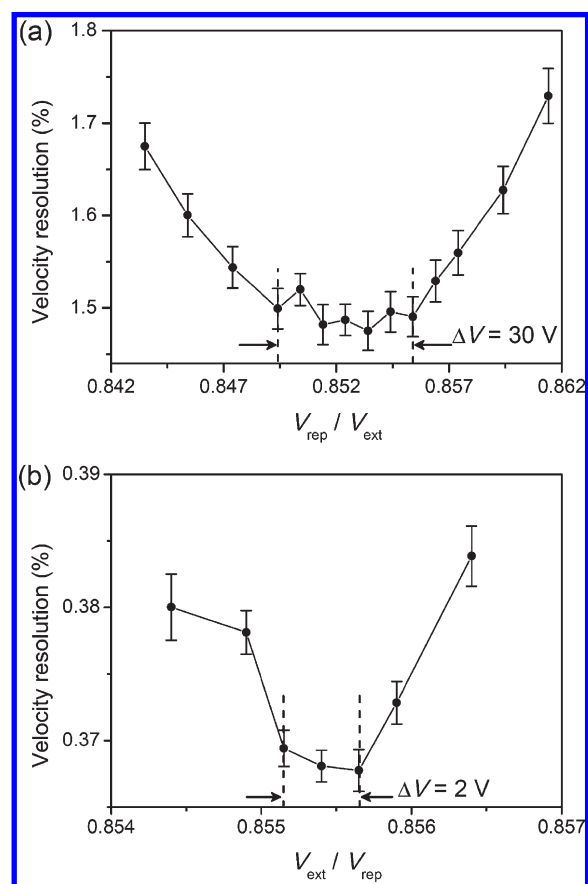
Figure 5. (a) Velocity resolution evaluated by PEI of Kr as a function of V_{ext}/V_{rep}. A low-resolution (512 × 512 pixels) CCD camera was used without image processing. Due to the low resolution of the camera, the focusing curve is broad. (b) Velocity resolution evaluated by PEI of Ar with a super-resolution (4096 × 4096 pixels) imaging system. The focusing curve is much sharper and the resolution profile for the V_{ext}/V_{rep} ratio is V-shaped. The error bars correspond to the fitting errors (fwhm).

to an energy resolution ($\Delta E/E = 2\Delta v/v$) of 2.9% at 7.22 eV. This resolution is insufficient to resolve the fine structure splitting of

Figure 6. PKE distributions determined by He I PEI of supersonic beams of Ar using a super-resolution (4096 × 4096 pixels) imaging system. The inset shows an expanded view in the PKE region between 5.1 and 5.6 eV. The solid line indicates the best-fit Gaussian to the observed data; it has a fwhm of 40 meV at 5.461 eV.

Ar (0.178 eV). Figure 5a shows the velocity resolution measured as a function of V_{ext}/V_{rep} by PEI of Kr using a standard CCD camera. It shows that the resolution varies gradually with V_{ext}/V_{rep} within the range of ca. 30 V about the best point. The broad focusing curve and poor velocity resolution, which go against the theoretical prediction, are attributed to the low imaging resolution. To examine the focusing curve more precisely, we used a super-resolution imaging system using a 2048 × 2048 pixel CCD camera.[25] We achieved an effective imaging resolution of 4096 × 4096 by performing a 2 × 2 subpixel centroiding calculation. Figure 5b shows the velocity resolution measured by super-resolution imaging of Ar as a function of V_{ext} (which was varied in 1 V steps) for V_{rep} and V_{port} fixed at −4000 and −3464.8 V, respectively. The response of the velocity resolution to the variation in V_{ext} is considerably sharper in this case; the resolution clearly degrades on both sides of the best point. The best voltage ratio V_{ext}/V_{rep} differs slightly for the two above-mentioned measurements because the two measurements employed slightly different flight lengths. At the optimal ratios of $V_{port}/V_{rep} = 0.8662$ and $V_{ext}/V_{rep} = 0.8557$, we obtained an energy resolution ($\Delta E/E$) of 0.735% at 5.461 eV (fwhm: 40 meV). This value is in excellent agreement with the energy resolution (0.72%) calculated from 500 electron trajectories with initial velocities parallel to the face of an MCP with 5.461 eV kinetic energy. The improved imaging resolution enabled the fine structure splitting of Ar to be resolved, as shown in Figure 6. In PEI experiments, the speed resolution Δv is limited by spatial resolution of the imaging system that is constant over the imaging area. Therefore, $\Delta v/v$ varies inversely proportional to v. The energy resolution $\Delta E/E$ is 2 times larger than $\Delta v/v$ by definition. Therefore, if the best energy resolution is 0.735% at 5.461 eV, it degrades to 7.35% at 0.546 eV.

With unpolarized light, the photoelectron angular distribution is cylindrically symmetric about the light propagation direction. We analyzed the angular distribution $[I(\theta)]$ using the standard formula for single-photon ionization with unpolarized light:

$$I(\theta) = \frac{\sigma}{4\pi}\left[1 + \frac{\beta}{2}\left(\frac{3}{2}\sin^2\theta - 1\right)\right]$$

where θ is the angle between the light propagation direction and the outgoing photoelectron velocity, σ is the integrated
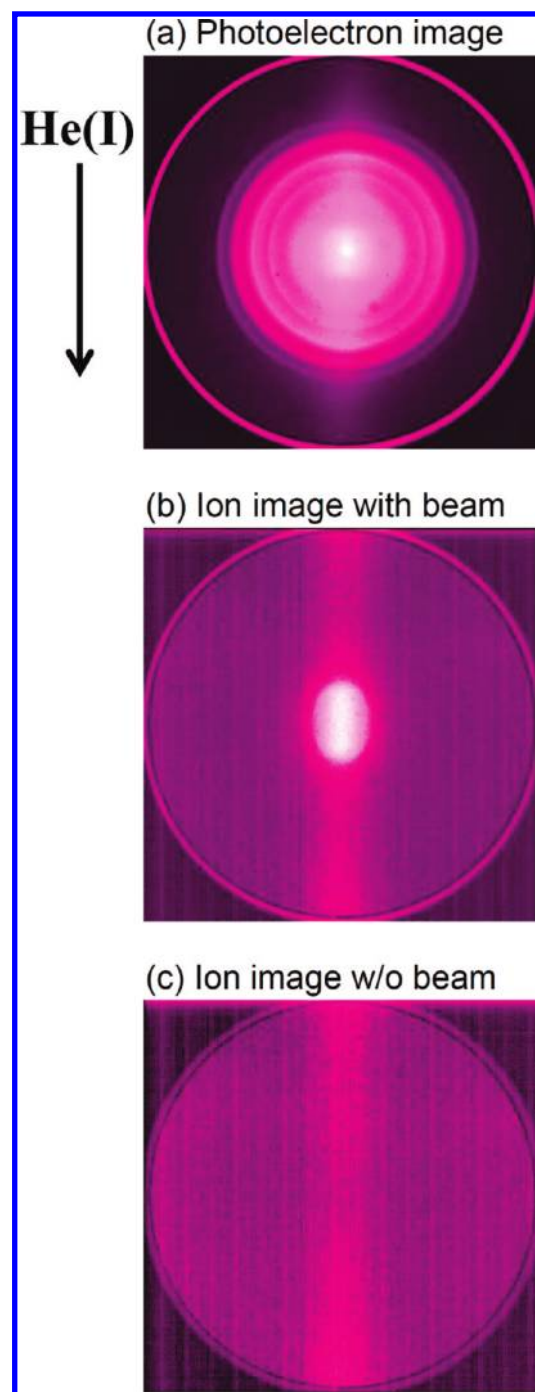
Figure 7. (a) Photoelectron image obtained for He I photoionization of a continuous supersonic beam of 8% benzene seeded in He (the background image has been subtracted). The vertical band along the VUV light path is due to photoionization of water vapor. (b) Ion image measured in space-mapping mode to trace the spatial region where the He I light beam intersects the supersonic molecular beam. (c) Ion image without the molecular beam. Comparison with (b) reveals that the bright elliptical spot in the center is due to benzene ions, whereas the vertical band along the propagation direction of the He I beam is due to residual water in the ionization chamber. The arrow indicates the propagation direction of the He I radiation.

ionization cross section, and β is the anisotropy parameter. We determined the anisotropy parameters for the $^2P_{3/2}$ and $^2P_{1/2}$ ionization channels of Kr to be 1.24 ± 0.01 and 1.21 ± 0.01
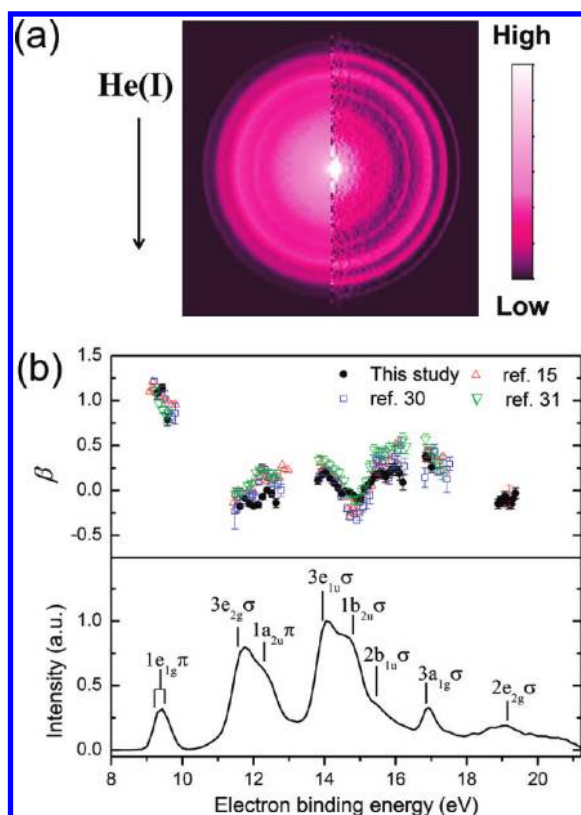
Figure 8. (a) Symmetrized photoelectron image of He I photoionization of a pulsed supersonic beam of 18% benzene seeded in He (the background image has been subtracted). The left half is the raw image and the right half is the slice image obtained by taking the inverse Abel transform. With unpolarized light, the axis of cylindrical symmetry is the propagation direction of the light (indicated by the arrow). The vertical band of the background signal observed with the continuous molecular beam was suppressed. (b) Energy-dependent anisotropy parameters β (upper panel, solid circle) and photoelectron spectrum (lower panel) obtained from (a). Since the kinetic energy of the photoelectron is proportional to the square of the radius in the slice image, the energy resolution limited by the pixel size of a CCD camera degrades at higher energies. Consequently, the energy widths considered for fitting β values were 60 and 140 meV in the region of binding energy around 19 and 9 eV, respectively. Data from Sell et al.,[30] Carlson et al.,[15] and Mattsson et al.[31] are given as open squares ($\square$), open triangles ($\triangle$), and open inverted triangles ($\triangledown$), respectively. The assignments of the ionized orbitals are indicated at the vertical ionization point.[15] The error bars are the fitting errors.

respectively, from a symmetrized image of the original Cartesian image. The errors are the fitting errors of the least-squares fit using the above equation. We also determined the anisotropy parameters independently for the four quadrants in the photoelectron image and obtained 1.26 ± 0.04 and 1.22 ± 0.08 for $^2P_{3/2}$ and $^2P_{1/2}$ respectively. The errors are the standard deviations of the anisotropy parameters determined from the four quadrants; the larger errors obtained using this approach result from the nonuniform sensitivity of the imaging detector. The anisotropy parameters of Kr determined by both methods are in good agreement with values given in the literature,[26-28] which indicates that symmetrization of the raw image prior to analysis does not affect the anisotropy parameter of our high-quality images and that it suppresses the effect of the nonuniform sensitivity of the detection system.

B. He I Photoelectron Imaging of Benzene and Pyridine.

On the basis of results for rare gases, we performed PEI experiments with polyatomic molecules in continuous supersonic molecular beams. However, we found that the signal level was not sufficiently stronger than the background photoionization signal of the residual water vapor in the photoionization chamber. The partial pressure of water in the ionization chamber was evaluated to be ca. 2×10^{-8} Torr using a residual gas analyzer (Stanford Research Systems, RGA200). Figure 7a shows a typical integrated photoelectron image obtained by He I photoionization of a continuous supersonic beam of 8% benzene in He with a stagnation pressure of 1.2 atm (the background image obtained without the molecular beam has been subtracted). The signal and background images had integration times of 100 min. The image contains a vertical band along the VUV light path due to photoionization of water vapor. The photoelectrons from water are visible in Figure 7a, because image subtraction did not completely eliminate the background signal due to the different conditions of the residual gas in the chamber with and without the molecular beam. Parts b and c of Figure 7 respectively show ion images observed with and without the molecular beam; mass selection was not performed. Comparison of these two figures suggests that the bright elliptical spot in the center is due to benzene ions, whereas the vertical band along the propagation direction of the He I light originates from water ions.

To enhance the contrast ratio between the signal and the background, we used a pulsed beam instead of a continuous molecular beam and we also increased the pumping rate by adding a turbomolecular pump (650 L/s) to the ionization chamber. The He I radiation continuously induces photoionization of the residual gas. We time-gated both the CCD and the MCP so as to detect photoelectrons only when a pulsed beam was introduced into the ionization region. A low-resolution CCD camera (512×512 pixels) was used for synchronization with an external trigger. As Figure 8a shows, pulsed operation considerably suppressed the background photoelectron from the residual water vapor. Both the signal and background images were integrated for 90 min at a repetition rate of 20 Hz (the maximum read-out rate of our CCD camera). As the vacuum system allows 100 Hz of gas pulses at a stagnation pressure of 0.55 atm, the duty cycle of our PEI system can be easily increased by a factor of 5 by not synchronizing the CCD camera.

Figure 8b shows the photoelectron spectrum and the energy-dependent anisotropy parameter measured for jet-cooled benzene. Benzene is the most fundamental aromatic molecule, and consequently it has been used as a benchmark system for UPS of polyatomic molecules.[14] As mentioned in the previous section, photoionization with unpolarized light generates a PAD that is cylindrically symmetric about the light propagation direction; therefore, a positive β corresponds to preferential ejection of electrons perpendicular to the symmetry axis, whereas a negative β corresponds to preferential ejection in the propagation direction. No signature from benzene dimers (electron binding energy = 8.65 eV)[29] is visible in our photoelectron spectrum. The modest resolution of 0.2−0.3 eV was too low to resolve vibrational structures. As Figure 8b shows, the energy-dependent anisotropy parameters determined in the present study are in excellent agreement with values given in the literature;[15,30,31] Table 1 tabulates and compares the numerical values with literature values.[15,30,31] In the first band $1e_{1g}(\pi)$, the anisotropy parameter decreases at high binding energies. Carlson and Anderson[14] have observed the same characteristic and suggested

2958

dx.doi.org/10.1021/jp1098574 |*J. Phys. Chem. A* 2011, 115, 2953–2965

Table 1. Electron Binding Energies (eV) and Anisotropy Parameters (β) for Benzene at 58.4 nm

	this study		Sell et al.[c]		Carlson et al.[d]		Mattsson et al.[f]	
orbital[a]	eBE	β	eBE	β	eBE	β	eBE	β
$1e_{1g}(\pi)$					9.11	1.11		
			9.21	1.21(3)	9.19	1.15	9.24	1.11(4)
	9.29	1.08(6)[b]	9.33	1.04(4)	9.30	1.10	9.34	0.97(5)
					9.38	1.06		
	9.44	1.14(5)	9.42	1.13(3)	9.48	1.05	9.44	0.90(4)
			9.51	1.02(9)	9.53	1.01	9.53	0.84(9)
	9.58	0.79(7)	9.60	0.85(7)	9.63	1.00	9.61	0.87(5)
			9.71	0.83(7)	9.72	0.96		
			9.80	0.86(12)	9.84	0.97		
$3e_{2g}(\sigma)$			11.48	−0.23(2)	11.46	−0.13	11.49	−0.04(4)
			11.53	−0.20(5)	11.59	−0.16	11.57	−0.01(2)
	11.62	−0.18(3)	11.62	−0.04(7)	11.64	−0.07		
	11.75	−0.09(2)	11.70	−0.11(6)	11.73	−0.03	11.67	−0.02(3)
			11.80	−0.04(5)	11.82	−0.04		
	11.88	−0.15(3)	11.90	−0.07(3)	11.90	0.02	11.84	0.06(2)
	12.01	−0.17(3)	11.98	−0.05(5)	12.00	0.03	11.95	0.08(2)
			12.08	−0.09(5)	12.05	0.09		
$1a_{2u}(\pi)$							12.07	0.20(3)
	12.13	−0.16(3)	12.16	0.09(2)	12.16	0.18	12.19	0.23(2)
	12.26	−0.07(2)	12.24	0.25(5)	12.25	0.18		
			12.33	0.23(3)	12.32	0.13	12.31	0.18(4)
	12.39	0.00(3)	12.42	0.15(9)	12.38	0.11	12.44	0.19(4)
	12.51	−0.04(4)	12.52	0.01(5)	12.49	0.15		
	12.63	−0.14(5)	12.60	0.14(5)	12.59	0.15	12.56	0.13(4)
			12.69	0.08(5)	12.65	0.16	12.68	0.19(4)
			12.77	0.00(7)	12.74	0.15		
					12.83	0.29		
					12.91	0.24		
					13.00	0.24		
$3e_{1u}(\sigma)$	13.82	0.11(4)	13.85	0.14(5)	13.89	0.20	13.85	0.34(5)
	13.93	0.17(3)	13.94	0.21(4)	14.00	0.25	14.00	0.32(6)
	14.04	0.20(2)	14.02	0.21(4)	14.06	0.22		
	14.15	0.14(2)	14.12	0.21(4)	14.17	0.20	14.14	0.28(5)
	14.26	0.08(2)	14.20	0.14(7)	14.26	0.19	14.27	0.23(5)
			14.30	0.11(2)	14.34	0.16		
	14.37	0.03(2)	14.38	0.07(5)	14.40	0.11	14.42	0.20(4)
	14.48	−0.03(2)	14.46	−0.05(5)	14.49	0.02		
$1b_{2u}(\sigma)$	14.59	−0.01(2)	14.55	−0.04(5)	14.58	−0.07	14.56	0.11(3)
			14.65	−0.20(4)	14.67	−0.20	14.68	−0.02(4)
	14.70	−0.01(2)	14.73	−0.29(4)	14.76	−0.24		
	14.81	−0.05(2)	14.83	−0.26(3)	14.84	−0.20	14.81	−0.11(4)
	14.91	−0.09(3)	14.91	−0.33(4)	14.94	−0.23	14.93	−0.10(4)
	15.02	−0.08(4)	14.99	−0.25(8)	14.98	−0.13		
			15.09	−0.19(5)	15.07	−0.07	15.05	0.00(5)
	15.12	0.02(4)	15.19	−0.08(13)	15.15	0.01	15.17	0.10(5)
	15.22	0.06(4)	15.27	−0.06(9)	15.25	0.02		
$2b_{1u}(\sigma)$	15.32	0.11(4)	15.35	0.30(10)	15.34	0.07	15.28	0.27(6)
	15.43	0.16(5)	15.46	0.34(8)	15.41	0.19	15.40	0.45(6)
	15.53	0.18(5)	15.53	0.33(14)	15.50	0.33	15.52	0.43(5)
	15.63	0.18(5)	15.62	0.32(7)	15.62	0.33	15.63	0.40(6)
	15.72	0.15(6)	15.70	0.39(10)	15.74	0.25	15.74	0.42(5)
	15.82	0.20(7)	15.81	0.14(7)	15.84	0.34	15.84	0.49(4)

2959

dx.doi.org/10.1021/jp1098574 |J. Phys. Chem. A 2011, 115, 2953–2965

Table 1. Continued

orbital[a]	this study		Sell et al.[c]		Carlson et al.[d]		Mattsson et al.[f]	
	eBE	β	eBE	β	eBE	β	eBE	β
	15.92	0.23(6)	15.90	0.32(8)	15.91	0.42		
	16.01	0.24(6)	15.98	0.38(12)	16.02	0.52	15.96	0.49(4)
			16.06	0.30(9)	16.07	0.52	16.07	0.46(5)
	16.11	0.19(8)	16.16	0.50(9)			16.19	0.57(7)
	16.20	0.09(9)	16.24	0.27(9)			16.30	0.49(8)
$3a_{1g}(\sigma)$	16.84	0.38(5)	16.83	0.14(11)			16.84	0.57(6)
	16.93	0.37(4)	16.91	0.45(4)	16.93	0.34	16.96	0.45(6)
	17.01	0.26(5)	16.99	0.38(7)	17.03	0.40		
			17.09	0.43(8)	17.07	0.37	17.07	0.39(9)
			17.19	0.21(4)	17.17	0.29	17.19	0.31(7)
			17.26	0.21(4)	17.25	0.33		
			17.34	0.30(10)	17.34	0.38	17.31	0.23(11)
			17.44	0.13(15)	17.42	0.21		
			17.52	0.30(8)				
$2e_{2g}(\sigma)$	18.89	−0.15(5)						
	18.95	−0.11(5)						
	19.01	−0.13(5)						
	19.07	−0.07(5)						
	19.13	−0.09(5)						
	19.19	−0.16(5)			19.20	−0.06(12)[e]		
	19.25	−0.15(5)						
	19.31	−0.09(6)						
	19.37	−0.03(6)						

[a] The orbital assignments for benzene are those in ref 15. [b] Errors (±, in last digit unless indicated otherwise) given in parentheses. [c] The energy-dependent anisotropy parameters are reproduced from ref 30. [d] The energy-dependent anisotropy parameters are reproduced from ref 15. [e] β was determined by integrating over the area of the $2e_{2g}$ (σ) band. [f] Reference 31.

that this variation may be due to the Jahn−Teller split states of D_0. However, the effect of Jahn−Teller splitting on the photoelectron anisotropy parameters has not been elucidated experimentally or theoretically.[32] Another possible origin for the variation in β is a Coulomb phase. Since β for photoionization from $1e_{1g}(\pi)$ increases with increasing PKE,[15,33,34] β is expected to diminish at higher binding energies (i.e., lower PKEs) within the first band. The highest-resolution He I photoelectron spectrum of benzene reported by Baltzer et al.[33] resolved the vibrational structure of $1e_{1g}(\pi)$ very clearly; unfortunately, however, β was not measured with a high vibrational resolution.

Figure 9 shows the results for pyridine 10% seeded in He. The energy-dependent photoelectron anisotropy parameters and photoelectron spectrum were obtained by taking the inverse Abel transform of the symmetrized image. The numerical values of β are tabulated and compared with values in the literature[35,36] in Table 2. We found that a microdischarge was generated in the MCP when a high density of neutral molecules impinged on the MCP; to prevent this, we restricted the stagnation pressure to 0.2 atm. Micro-discharges have not been observed in other PEI spectrometers in our laboratory; they appear to be a specific problem of this detector. The low stagnation pressure of 0.2 atm necessitated using a long (3 h) integration time for pyridine for each signal and background image. Microdischarges could be completely eliminated by rede-signing the PEI spectrometer for a molecular beam traveling parallel to the face of the imaging detector.

The first band between 9.2 and 10.2 eV corresponds to ioniza-tion to D_0 and D_1 and the second band near 10.6 eV is assigned to
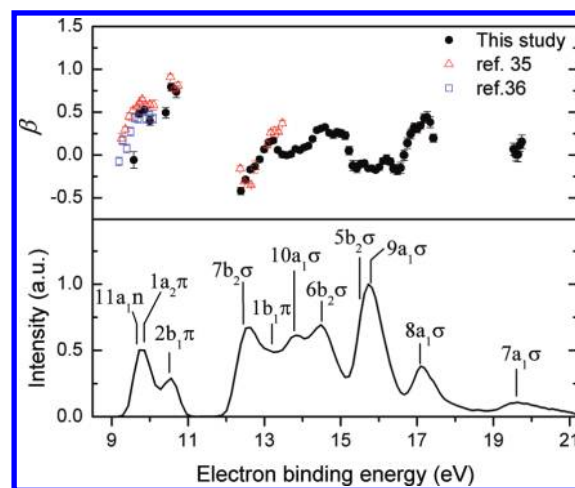
Figure 9. Energy-dependent anisotropy parameter β (upper panel, solid circles) and photoelectron spectra (lower panel) obtained from He I photoionization of pulsed supersonic beams of 10% pyridine seeded in He. The image was symmetrized and the background image was subtracted prior to data analysis. Data from Piancastelli et al.[36] and Utsunomiya et al.[35] are given as open squares (□) and open triangles (△), respectively. Assignments of the ionized orbitals are indicated at the vertical ionization point.[41] The error bars are the fitting errors.

D_2. D_0 and D_1 are due to electron removal from either $11a_1(n)$ or $1a_2(\pi)$ orbitals; however, the ordering of these two states is controversial. ADC(3) Green function calculations[37] predict a

Table 2. Electron Binding Energies (eV) and Anisotropy Parameters (β) for Pyridine at 58.4 nm

orbital[a]	this study		Utsunomiya et al.[c]		Piancastelli et al.[d]	
	eBE	β	eBE	β	eBE	β
$11a_1(n), 1a_2(\pi)$			9.26	0.19(6)	9.20	−0.08(5)
			9.36	0.30(3)	9.30	0.17(5)
			9.46	0.45(4)	9.40	0.07(5)
	9.58	−0.06(10)[b]	9.56	0.52(3)	9.50	0.27(5)
			9.66	0.56(1)	9.60	0.43(5)
	9.72	0.48(3)	9.73	0.61(1)	9.70	0.42(5)
	9.86	0.53(3)	9.80	0.65(2)	9.80	0.51(5)
			9.90	0.58(2)	9.90	0.42(5)
	10.00	0.40(5)	10.00	0.59(3)	10.00	0.47(5)
			10.10	0.58(6)	10.10	0.42(5)
$2b_1(\pi)$	10.42	0.49(6)				
	10.56	0.79(4)	10.54	0.91(3)		
	10.69	0.73(7)	10.64	0.77(2)		
			10.74	0.81(4)		
$7b_2(\sigma)$	12.39	−0.42(4)	12.37	−0.16(3)		
	12.51	−0.29(3)	12.48	−0.31(1)		
	12.63	−0.17(3)	12.65	−0.35(1)		
	12.75	−0.13(3)	12.75	−0.14(7)		
	12.88	−0.05(3)				
$1b_1(\pi)$	13.00	0.07(3)	13.07	0.12(4)		
	13.12	0.15(3)	13.17	0.26(3)		
	13.23	0.17(3)	13.27	0.27(6)		
	13.35	0.06(3)	13.37	0.27(2)		
	13.47	0.00(3)	13.47	0.37(3)		
	13.59	0.00(3)				
$10a_1(\sigma)$	13.70	0.01(3)				
	13.82	0.07(2)				
	13.93	0.06(2)				
	14.04	0.09(3)				
	14.15	0.11(3)				
$6b_2(\sigma)$	14.26	0.19(3)				
	14.37	0.29(2)				
	14.48	0.31(2)				
	14.59	0.32(2)				
	14.70	0.26(3)				
	14.81	0.23(4)				
	14.91	0.26(4)				
	15.02	0.25(4)				
	15.12	0.23(5)				
$5b_2(\sigma), 9a_1(\sigma)$	15.22	0.05(5)				
	15.32	−0.13(6)				
	15.43	−0.15(5)				
	15.53	−0.11(4)				
	15.63	−0.10(3)				
	15.72	−0.16(2)				
	15.82	−0.16(3)				
	15.92	−0.18(3)				
	16.01	−0.14(4)				
	16.11	−0.07(4)				
	16.20	−0.04(4)				
	16.30	−0.08(4)				
	16.39	−0.16(5)				

Table 2. Continued

	this study		Utsunomiya et al.[c]		Piancastelli et al.[d]	
orbital[a]	eBE	β	eBE	β	eBE	β
	16.48	−0.18(5)				
	16.57	−0.15(7)				
$8a_1\ (\sigma)$	16.66	0.00(6)				
	16.75	0.14(6)				
	16.84	0.25(6)				
	16.93	0.32(5)				
	17.01	0.30(4)				
	17.10	0.35(4)				
	17.18	0.43(5)				
	17.27	0.44(6)				
	17.35	0.38(6)				
	17.43	0.20(5)				
$7a_1(\sigma)$	19.54	0.07(7)				
	19.59	0.01(8)				
	19.64	0.00(8)				
	19.69	0.11(7)				
	19.75	0.15(8)				

[a] The orbital assignments for pyridine are those made in ref 41. [b] Errors (±, in last digit unless indicated otherwise) given in parentheses. [c] Reference 35. [d] The energy-dependent anisotropy parameters are reproduced from ref 36.

$\pi-n-\pi$ ordering, which is similar to the results of the Green function[38,39] and valence bond methods.[40] However, more recent calculations using SAC−CI,[41] DFT-TP,[42] CASPT2,[43] and MRDCI[44] suggest an $n-\pi-\pi$ ordering. MRDCI predicted that the first two ionic states have an energy difference of 0.7 eV, whereas the other methods have given differences only less than 0.2 eV. In 1978, Utsunomiya et al.[35] attempted to determine the ordering of these two states using He I photoelectron spectroscopy; they compared the anisotropy parameters with those of 2,6-lutidine (dimethylpyridine) for which spectroscopic assignments have been well established. Utsunomiya et al. observed that the anisotropy parameter was ca. 0.2 near the ionization threshold, whereas it increased to ca. 0.6 in the middle of the first band. On the basis of this, they assigned D_0 of pyridine to the n^{-1} state, since the n^{-1} state of 2,6-lutidine has a low β. Piancastelli et al.[36] have performed similar measurements with synchrotron radiation but they varied the photon energy. They found that the anisotropy parameter increased when the photon energy was increased from 13 to 27 eV and that the higher binding energy region of the first band exhibited a more rapid increase in β than the lower binding energy region. On the basis of this, they also assigned D_0 to the n^{-1} state and D_1 to the π^{-1} state.

He I UPS creates PKEs of ca. 10 eV in ionization to D_0 and D_1. In this PKE region, the photoelectron anisotropy parameter increases slowly with increasing PKE due to the energy-dependent Coulomb phases.[34] In contrast, the present study and the results of Utsunomiya et al. reveal that the anisotropy parameter increases within the first band with increasing binding energy (i.e., decreasing PKE). This suggests that the variation of β in the first band is not due to Coulomb phases but rather it is due to D_1 being located close to D_0; the contribution of D_1 increases rapidly in the first band causing β to increase. CMSXα calculations[34] predict that β is almost zero at a PKE of ~5 eV for both ionization to D_0 and D_1 but that it increases with increasing PKE; this explains the results of Piancastelli et al.[36] The origin band of

D_1 has not been determined yet. Appendix A shows a high-resolution He I spectrum of jet-cooled pyridine measured in our laboratory with a hemispherical energy analyzer.

The fourth and fifth bands between 12.5 and 13.5 eV have been assigned to $7b_2\sigma$ and $1b_1\pi$, respectively.[35] As far as we know, anisotropy parameters for electron binding energies of over 14 eV have not been reported. All these cation states are due to the removal of an electron from the σ orbitals (see Figure 9). There are two different theoretical assignments for the overlapping bands within 0.3 at 15.8 eV. These bands are associated with the $9a_1(\sigma)$ C−H and $5b_2(\sigma)$ C−C bonding orbitals. All the calculations that predict $n-\pi-\pi$ ordering for the first three cation states suggest $5b_2(\sigma) < 9a_1(\sigma)$, whereas the other methods that support $\pi-n-\pi$ ordering for the first three states suggest the opposite result, $5b_2(\sigma) > 9a_1(\sigma)$. The assignments in Figure 9 follow the former assignment.

C. Comparison of PEI with He I and SASE-FEL. We have used the above-mentioned VUV-PEI spectrometer in photoionization experiments using a VUV free electron laser (SCSS: SPring-8 Compact SASE Source).[45] As mentioned before, the resolutions of PEI using He I is limited by the ionization volume, whereas SCSS is free from this problem since the laser beam is focused down to a diameter of ca. 0.1 mm. Our trajectory calculations indicate that the energy resolution $\Delta E/E$ of our charged particle optics will be 0.04% at 5.461 eV for a small ionization volume created by a laser, which is close to the ultimate resolution, 0.06%, obtainable using the best commercially available MCP that is 70 mm in diameter and has 10 μm pores. In practice, however, we found that the resolution is superior with He I radiation than FEL radiation at 58.4 nm (Figure S1 in the Supporting Information), although the former has a much larger ionization volume. This is because SCSS, like other FELs, uses self-amplified spontaneous emission (SASE) of radiation that has unavoidable fluctuations in the spectrum, resulting in a large effective bandwidth of 0.1 eV.[18]

Table A. Vibrational Assignments of the Bands in Figure 11

no.	eBE (eV)	exptl vibr energy (meV)	assignment	calcd vibr energy (meV)	Δ (meV)[a]
1	9.199	0	$0-0$		
2	9.273	74	10_0^1	74	0
3	9.318	119	9_0^1	119	0
4	9.348	149	10_0^2	148	−1
5	9.3925	193.5	$9_0^1 10_0^1$	193	−0.5
6	9.419	220	10_0^3	223	3
7	9.428	229	9_0^2	238	9
8	9.467	268	$9_0^1 10_0^2$	267	−1
9	9.487	288	10_0^4	294	6
10	9.504	305	$9_0^2 10_0^1$	303	−2
11	9.541	342	$9_0^1 10_0^3$	342	0
12	9.555	356	9_0^3	357	1
13	9.579	380	$9_0^2 10_0^2$	379	−6
14	9.589	390	unknown		
15	9.61	411	$9_0^1 10_0^4$	416	5
16	9.626	427	$9_0^3 10_0^1$	431	4
17	9.644	445	$9_0^2 10_0^3$	454	9
18	9.662	463	not sure		
19	9.697	498	$9_0^3 10_0^2$	501	3
20	9.724	525	$9_0^2 10_0^4$	537	12

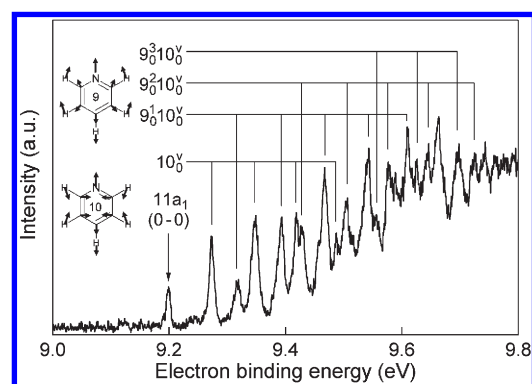[a] Δ = (calcd vibr energy) − (exptl vibr energy).
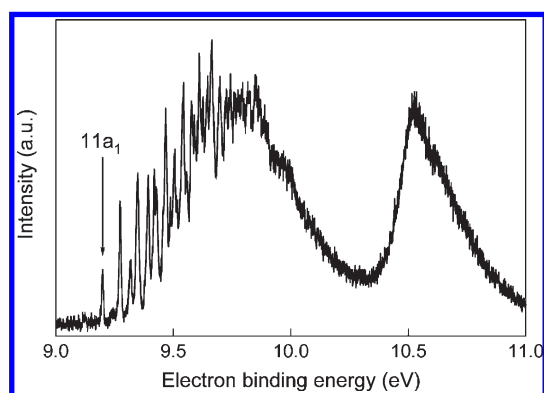
Figure 10. He I photoelectron spectrum of jet-cooled pyridine measured with a hemispherical energy analyzer. The two bands with lowest electron binding energies are shown. He I radiation was unpolarized and photoelectrons were detected in the perpendicular direction with respect to the light propagation axis. The band indicated by "11a$_1$" is the origin band of the $D_0(n^{-1}) \leftarrow S_0$ transition. The broad feature suggests that $D_1(\pi^{-1})$ due to an electron removal from the 1a$_2$ orbital exists within this band; however, its origin is currently unclear.

Figure 11. Expanded view of the He I photoelectron spectrum shown in Figure 10. The combination bands of the modes 9 and 10 (in-plane totally symmetric vibrations) are indicated.

VUV-FEL has the advantage of providing much more intense radiation than He I. However, the pulse energy of the SCSS radiation was too high for single-photon ionization experiments; we had to use metal and gas filters to reduce it in our experiment. Since SCSS is operated at a low repetition rate (10−60 Hz), this reduction in the pulse energy diminishes the advantage of VUV-FEL over He I for UPS.

Since the VUV-FEL beam is tightly focused, we anticipated that background photoelectrons have a much smaller influence than for He I. However, we found that the conventional three-plate electrostatic lens[23] generated considerable background electrons

with SCSS. Our new lens system was essential in obtaining high-quality electron images with SCSS.

■ SUMMARY

We described He I UPS in the new form of PEI. The performance of He I PEI was examined by observing photoionization of rare gas atoms and polyatomic molecules. We demonstrated that time-gated measurement with a pulsed beam provides a high signal contrast relative to the background from water vapor in the ionization chamber. The photoelectron anisotropy parameters determined for benzene and pyridine were in good agreement with values given in the literature. Real-time subpixel centroiding calculations achieved the best energy resolution of 0.735% at 5.461 eV, which corresponds to a fwhm of 40 meV. This does not represent the ultimate resolution achievable with the spectrometer. It is possible to increase the resolution by 1 order of magnitude by tightly focusing the photon

beam. The CCD imaging detector in our instrument could be replaced by a delay line detector; however, the resolution obtainable is comparable with that of a standard CCD camera. The highest imaging resolution is obtained by using a high-resolution camera and super-resolution image processing. However, it requires a high-frame-rate camera to avoid spatial overlapping between two electron impacts on the detector. In addition, either high-speed real-time image processing to calculate the center of gravity for each light spot or a large memory to store images for off-line analysis after the measurement are required. Our super-resolution imaging system is currently able to handle up to 256 light spots in a single frame (30 frames/s), which is too low for He I UPS. This problem will be solved when imaging devices with higher frame rates and more rapid digital image processing become available.

■ APPENDIX A: VIBRONIC STRUCTURE OF THE FIRST BAND OF PYRIDINE

Innes et al.[46] reviewed the electronic excited states of azabenzenes and azanaphthalenes. They state that the adiabatic ionization energy of pyridine is 9.197 eV in the text but 74 740 cm^{-1} (9.267 eV) in their Table 7. The former value is from photoelectron spectroscopy of pyridine vapor by Reineck et al. (9.197 eV) in 1982,[47] whereas the latter value is probably from an earlier work by Turner (9.26 eV) in 1970.[48] Bolovinos et al. used 9.26 eV in their analysis of Rydberg state spectroscopy,[49] whereas later studies such as that by Walker et al.[44] took the ionization energy of pyridine to be 9.197 eV. The difficulty in determining the ionization energy is due to the small Franck−Condon factor of the 0−0 band, which is similar to the case of pyrazine that we previously studied.[13]

Figure 10 shows the He I photoelectron spectrum of jet-cooled pyridine measured in our laboratory with a hemispherical energy analyzer at a resolution of 10 meV. The overall features of this spectrum are in excellent agreement with those by Reineck et al.[47] The D_1 state is thought to be close to the D_0 state; for instance, SAC-CI calculations predict D_0 and D_1 to be 9.23 and 9.36, respectively.[41] This proximity is regarded as the cause of the spectral complexity of the first band; however, the origin of D_1 has not been established.

Figure 11 shows an expanded view of the first band. The vibrational progressions of the mode 10 are clearly identified. Riese et al. have performed mass-analyzed threshold ionization (MATI) spectroscopy of pyridine and deduced 74 185 ± 6 cm^{-1} (9.1978 ± 0.0008 eV).[50] MATI was performed within an excess vibrational energy of 0.2 eV from the origin. No examination has been reported for the binding energy region >9.4 eV where a broad background appears in UPS. Table A lists the vibrational assignments for the spectrum. Notice that the first cold vibrational band 10_0^1 is at 9.273 eV, which is regarded as the source of the old value (9.26 eV) of the ionization energy. This illustrates the difficulty in experimentally determining the lowest cold band.

As for the Franck−Condon factor from S_0, there is an interesting difference for the 3s Rydberg state. Turner et al. have performed (2+1) REMPI spectroscopy of pyridine via 3s Rydberg state in which they observed an intense band at 50 413 cm^{-1} (6.25 eV), and they assigned it to the 0−0 band.[51] Dion and Bernstein repeated the experiment in 1995,[52] and they observed the same band at 50 685 cm^{-1} (6.28 eV). Tsubouchi and Suzuki have performed (1+2′) REMPI photoelectron spectroscopy using a femtosecond laser and observed the photoelectron signal

attributed to ionization via the 3s state.[53] The photoelectron kinetic energy (PKE) they observed is related to the term value (T) of the Rydberg state as follows:

$$T = \text{PKE} + \text{IE} - h\nu_{\text{probe}}$$

where IE is the ionization energy and $h\nu_{\text{probe}}$ is the photon energy. Using an IE of 9.20 eV, T is calculated to be 6.27 eV. Thus, the assignment of the 3s state has been established. Notice that the maximum of the Franck−Condon envelope in UPS appears at higher vibronic levels than the 0−0 band (Figures 10 and 11), which contradicts the fact that two-photon excitation to the 3s state exhibited an intensity maximum in the 0−0 band. In the case of pyrazine, we found that the energy gaps between $D_1(\pi^{-1}) - D_0(n^{-1})$ and $3s(\pi^{-1}) - 3s(n^{-1})$ are different. It may be that the proximity effect between the $3s(n^{-1})$ and $3s(\pi^{-1})$ states of pyridine differs from that between $D_0(n^{-1})$ and $D_1(\pi^{-1})$, which gives rise to different Franck−Condon factors for the 3s and D_0 from S_0.

■ ASSOCIATED CONTENT

ⓢ Supporting Information. Comparison of photoelectron kinetic energy distribution of Kr in photoionization by He I radiation and FEL radiation and chromatic aberration of electrostatic lenses. This material is available free of charge via the Internet at http://pubs.acs.org.

■ AUTHOR INFORMATION

Corresponding Author
*E-mail: suzuki@kuchem.kyoto-u.ac.jp.

Present Addresses
⊥Department of Chemistry, Graduate School of Science and Engineering, Tokyo Metropolitan University, 1-1 Minami-Osawa, Hachioji, Tokyo 192-0397, Japan

■ ACKNOWLEDGMENT

■ REFERENCES

(1) Vilesov, F. I.; Kurbatov, B. L.; Terrenin, A. N. *Soviet Phys. (Doklady)* **1961**, *6*, 490.
(2) Turner, D. W.; AI-Jobory, M. I. *J. Chem. Phys.* **1962**, *37*, 3007.
(3) Koopmans, T. C. *Physica* **1933**, *1*, 104.
(4) Eland, J. H. D. *Photoelectron Spectroscopy*; Butterworth: London, 1974.
(5) Baltzer, P.; Karlsson, L.; Lundqvist, M.; Wannberg, B. *Rev. Sci. Instrum.* **1993**, *64*, 2179.
(6) Pollard, J. E.; Trevor, D. J.; Lee, Y. T.; Shirley, D. A. *Rev. Sci. Instrum.* **1981**, *52*, 1837.
(7) Öhrwall, G.; Baltzer, P.; Bozek, J. *Phys. Rev. Lett.* **1998**, *81*, 546.
(8) Öhrwall, G.; Baltzer, P.; Bozek, J. *Phys. Rev. A.* **1999**, *59*, 1903.
(9) Jarvis, G. K.; Song, Y.; Ng, C. Y.; Grant, E. R. *J. Chem. Phys.* **1999**, *111*, 9568.
(10) Merkt, F.; Osterwalder, A.; Seiler, R.; Signorell, R.; Palm, H.; Schmutz, H.; Gunzinger, R. *J. Phys. B, At. Mol. Opt. Phys.* **1998**, *31*, 1705.
(11) Schlag, E. W. *Zeke Spectroscopy*; Cambridge University Press: Cambridge, 1998.
(12) Müller-Dethlefs, K.; Schlag, E. W.; Grant, E. R.; Wang, K.; McKoy, B. V. *Adv. Chem. Phys.* **1995**, *90*, 1.

(13) Oku, M.; Hou, Y.; Xing, X.; Reed, B.; Xu, H.; Chang, C.; Ng, C. Y.; Nishizawa, K.; Ohshimo, K.; Suzuki, T. *J. Phys. Chem. A* **2008**, *112*, 2293.

(14) Carlson, T. A.; Anderson, C. P. *Chem. Phys. Lett.* **1971**, *10*, 561.

(15) Carlson, T. A.; Gerard, P.; Krause, M. O.; Grimm, F. A.; Pullen, B. P. *J. Chem. Phys.* **1987**, *86*, 6918.

(16) Suzuki, T. *Annu. Rev. Phys. Chem.* **2006**, *57*, 555.

(17) Ayvazyan, V.; Baboi, N.; Bahr, J.; Balandin, V.; Beutner, B.; Brandt, A.; Bohnet, I.; Bolzmann, A.; Brinkmann, R.; Brovko, O. I.; Carneiro, J. P.; Casalbuoni, S.; Castellano, M.; Castro, P.; Catani, L.; Chiadroni, E.; Choroba, S.; Cianchi, A.; Delsim-Hashemi, H.; Di Pirro, G.; Dohlus, M.; Dusterer, S.; Edwards, H. T.; Faatz, B.; Fateev, A. A.; Feldhaus, J.; Flottmann, K.; Frisch, J.; Frohlich, L.; Garvey, T.; Gensch, U.; Golubeva, N.; Grabosch, H. J.; Grigoryan, B.; Grimm, O.; Hahn, U.; Han, J. H.; Hartrott, M. V.; Honkavaara, K.; Huning, M.; Ischebeck, R.; Jaeschke, E.; Jablonka, M.; Kammering, R.; Katalev, V.; Keitel, B.; Khodyachykh, S.; Kim, Y.; Kocharyan, V.; Korfer, M.; Kollewe, M.; Kostin, D.; Kramer, D.; Krassilnikov, M.; Kube, G.; Lilje, L.; Limberg, T.; Lipka, D.; Lohl, F.; Luong, M.; Magne, C.; Menzel, J.; Michelato, P.; Miltchev, V.; Minty, M.; Moller, W. D.; Monaco, L.; Muller, W.; Nagl, M.; Napoly, O.; Nicolosi, P.; Nolle, D.; Nunez, T.; Oppelt, A.; Pagani, C.; Paparella, R.; Petersen, B.; Petrosyan, B.; Pfluger, J.; Piot, P.; Plonjes, E.; Poletto, L.; Proch, D.; Pugachov, D.; Rehlich, K.; Richter, D.; Riemann, S.; Ross, M.; Rossbach, J.; Sachwitz, M.; Saldin, E. L.; Sandner, W.; Schlarb, H.; Schmidt, B.; Schmitz, M.; Schmuser, P.; Schneider, J. R.; Schneidmiller, E. A.; Schreiber, H. J.; Schreiber, S.; Shabunov, A. V.; Sertore, D.; Setzer, S.; Simrock, S.; Sombrowski, E.; Staykov, L.; Steffen, B.; Stephan, F.; Stulle, F.; Sytchev, K. P.; Thom, H.; Tiedtke, K.; Tischer, M.; Treusch, R.; Trines, D.; Tsakov, I.; Vardanyan, A.; Wanzenberg, R.; Weiland, T.; Weise, H.; Wendt, M.; Will, I.; Winter, A.; Wittenburg, K.; Yurkov, M. V.; Zagorodnov, I.; Zambolin, P.; Zapfe, K. *Eur. Phys. J. D* **2006**, *37*, 297.

(18) Shintake, T.; Tanaka, H.; Hara, T.; Tanaka, T.; Togawa, K.; Yabashi, M.; Otake, Y.; Asano, Y.; Bizen, T.; Fukui, T.; Goto, S.; Higashiya, A.; Hirono, T.; Hosoda, N.; Inagaki, T.; Inoue, S.; Ishii, M.; Kim, Y.; Kimura, H.; Kitamura, M.; Kobayashi, T.; Maesaka, H.; Masuda, T.; Matsui, S.; Matsushita, T.; Maréchal, X.; Nagasono, M.; Ohashi, H.; Ohata, T.; Ohshima, T.; Onoe, K.; Shirasawa, K.; Takagi, T.; Takahashi., S; Takeuchi, M.; Tamasaku, K.; Tanaka, R.; Tanaka, Y.; Tanikawa, T.; Togashi, T.; Wu, S.; Yamashita, A.; Yanagida, K.; Zhang, C.; Kitamura, H.; Ishikawa, T. *Nat. Photonics* **2008**, *2*, 555.

(19) Barty, A.; Soufli, R.; McCarville, T.; Baker, S. L.; Pivovaroff, M. J.; Stefan, P.; Bionta, R. *Opt. Express* **2009**, *17*, 15508.

(20) Pfeifer, T.; Spielmann, C.; Gerber, G. *Rep. Prog. Phys.* **2006**, *69*, 443.

(21) Krausz, F.; Ivanov, M. *Rev. Mod. Phys.* **2009**, *81*, 163.

(22) Nisoli, M.; Sansone, G. *Prog. Quantum Electron.* **2009**, *33*, 17.

(23) Eppink, A. T. J. B.; Parker, D. H. *Rev. Sci. Instrum.* **1997**, *68*, 3477.

(24) Lin, J. J.; Zhou, J.; Shiu, W.; Liu, K. *Rev. Sci. Instrum.* **2003**, *74*, 2495.

(25) Ogi, Y.; Kohguchi, H.; Niu, D.; Ohshimo, K.; Suzuki, T. *J. Phys. Chem. A* **2009**, *113*, 14536.

(26) Kreile, J.; Kurland, H. D.; Seibel, W.; Schweig, A. *Nucl. Instrum. Methods* **1991**, *308*, 621.

(27) Kreile, J.; Schweig, A. *J. Electron Spectrosc. Relat. Phenom.* **1980**, *20*, 191.

(28) Karlsson, L.; Mattson, L.; Jadrny, R.; Siegbahn, K.; Thimm, K. *Phys. Lett. A* **1976**, *58*, 381.

(29) Krause, H.; Ernstberger, B.; Neusser, H. J. *Chem. Phys. Lett.* **1991**, *184*, 411.

(30) Sell, J. A.; Kuppermann, A. *Chem. Phys.* **1978**, *33*, 367.

(31) Mattsson, L.; Karlsson, L.; Jadrny, R.; Siegbahn, K. *Phys. Scr.* **1977**, *16*, 221.

(32) Shiromaru, H.; Katsumata, S. *Bull. Chem. Soc. Jpn.* **1984**, *57*, 3543.

(33) Baltzer, P.; Karlsson, L.; Wannberg, B.; Öhrwall, G.; Holland, D. M. P.; MacDonald, M. A.; Hayes, M. A.; von Niessen, W. *Chem. Phys.* **1997**, *224*, 95.

(34) Suzuki, Y.; Suzuki, T. *J. Phys. Chem. A* **2008**, *112*, 402.

(35) Utsunomiya, C.; Kobayashi, T.; Nagakura, S. *Bull. Chem. Soc. Jpn.* **1978**, *51*, 3482.

(36) Piancastelli, M. N.; Keller, P. R.; Taylor, J. W.; Grimm, F. A.; Carlson, T. A. *J. Am. Chem. Soc.* **1983**, *105*, 4235.

(37) Moghaddam, M. S.; Bawagan, A. D. O.; Tan, K. H.; von Niessen, W. *Chem. Phys.* **1996**, *207*, 19.

(38) von Niessen, W.; Diercksen, G. H. F.; Cederbaum, L. S. *Chem. Phys.* **1975**, *10*, 345.

(39) von Niessen, W.; Kraemer, W. P.; Diercksen, G. H. F. *Chem. Phys.* **1979**, *46*, 113.

(40) Tantardini, G. F.; Simonetta, M. *Int. J. Quantum Chem.* **1981**, *20*, 705.

(41) Wan, J.; Hada, M.; Ehara, M.; Nakatsuji, H. *J. Chem. Phys.* **2001**, *114*, 5117.

(42) Plashkevych, O.; Ågren, H.; Karlsson, L.; Pettersson, L. G. M. *J. Electron Spectrosc. Relat. Phenom.* **2000**, *106*, 51.

(43) Lorentzon, J.; Fülscher, M. P.; Roos, B. O. *Theor. Chim. Acta* **1995**, *92*, 67.

(44) Walker, I. C.; Palmer, M. H.; Hopkirk, A. *Chem. Phys.* **1990**, *141*, 365.

(45) Liu, S. Y.; Ogi, Y.; Fuji, T.; Nishizawa, K.; Horio, T.; Mizuno, T.; Kohguchi, H.; Nagasono, M.; Togashi, T.; Tono, K.; Yabashi, M.; Senba, Y.; Ohashi, H.; Kimura, H.; Ishikawa, T.; Suzuki, T. *Phys. Rev. A* **2010**, *81*, 031403.

(46) Innes, K. K.; Ross, I. G.; Moomaw, W. R. *J. Mol. Spectrosc.* **1988**, *132*, 492.

(47) Reineck, I.; Maripuu, R.; Veenhuizen, H.; Karlsson, L.; Siegbahn, K.; Powar, M. S.; Zu, W. N.; Rong, J. M.; Al-Shamma, S. H. *J. Elec. Spectrosc. Relat. Phenom.* **1982**, *27*, 15.

(48) Turner, D. W. *Molecular Photoelectron Spectroscopy*; Wiley: New York, 1970; p 323.

(49) Bolovinos, A.; Tsekeris, P.; Philis, J.; Pantos, E.; Andritsopoulos, G. *J. Mol. Spectrosc.* **1984**, *103*, 240.

(50) Riese, M.; Altug, Z.; Grotemeyer, J. *Phys. Chem. Chem. Phys.* **2006**, *8*, 4441.

(51) Turner, R. E.; Vaida, V.; Molini, C. A.; Berg, J. O.; Parker, D. H. *Chem. Phys.* **1978**, *28*, 47.

(52) Dion, C. F.; Bernstein, E. R. *J. Chem. Phys.* **1995**, *103*, 4907.

(53) Tsubouchi, M.; Suzuki, T. *J. Phys. Chem. A* **2003**, *107*, 10897.

(54) Ureña, F. P.; Gómez, M. F.; González, J. J. L.; Torres, E. M. *Spectrocim. Acta A* **2003**, *59*, 2815.